Mechanical and bio-corrosion properties of quaternary Mg–Ca–Mn–Zn alloys compared with binary Mg–Ca alloys

H.R. Bakhsheshi-Rad [a,*], M.H. Idris [a], M.R. Abdul-Kadir [b], A. Ourdjini [a], M. Medraj [c], M. Daroonparvar [a], E. Hamzah [a]

[a] Department of Materials Engineering, Faculty of Mechanical Engineering, Universiti Teknologi Malaysia, 81310 Johor Bahru, Johor, Malaysia
[b] Department of Biomechanics & Biomedical Materials, Faculty of Biomedical Engineering & Health Sciences, Universiti Teknologi Malaysia, 81310 Johor Bahru, Johor, Malaysia
[c] Department of Mechanical Engineering, Concordia University, 1455 De Maisonneuve Blvd. West, Montreal, QC H3G 1M8, Canada

ABSTRACT

Binary Mg–xCa alloys and the quaternary Mg–Ca–Mn–xZn were studied to investigate their bio-corrosion and mechanical properties. The surface morphology of specimens was characterized by X-ray diffraction (XRD), Fourier-transformed infrared spectroscopy (FTIR), scanning electron microscopy (SEM) and energy dispersive X-ray spectroscopy (EDS). The results of mechanical properties show that the yield strength (YS), ultimate tensile strength (UTS) and elongation of quaternary alloy increased significantly with the addition of zinc (Zn) up to 4 wt.%. However, further addition of Zn content beyond 4 wt.% did not improve yield strength and ultimate tensile strength. In contrast, increasing calcium (Ca) content has a deleterious effect on binary Mg–Ca alloys. Compression tests of the magnesium (Mg) alloys revealed that the compression strength of quaternary alloy was higher than that of binary alloy. However, binary Mg–Ca alloy showed higher reduction in compression strength after immersion in simulated body fluid. The bio-corrosion behaviour of the binary and quaternary Mg alloys were investigated using immersion tests and electrochemical tests. Electrochemical tests shows that the corrosion potential (E_{corr}) of binary Mg–2Ca significantly shifted toward nobeler direction from −1996.8 to −1616.6 mV$_{SCE}$ with the addition of 0.5 wt.% manganese (Mn) and 2 wt.% Zn content. However, further addition of Zn to 7 wt.% into quaternary alloy has the reverse effect. Immersion tests show that the quaternary alloy accompanied by two secondary phases presented higher corrosion resistance compared to binary alloys with single secondary phase. The degradation behaviour demonstrates that Mg–2Ca–0.5Mn–2Zn alloy had the lowest degradation rate among quaternary alloys. In contrast, the binary Mg–2Ca alloy demonstrated higher corrosion rates, with Mg–4Ca alloy having the highest rating. Our analysis showed the Mg–2Ca–0.5Mn–2Zn alloy with suitable mechanical properties and excellent corrosion resistance can be used as biodegradable implants.

© 2013 Elsevier Ltd. All rights reserved.

1. Introduction

A fascinating research topics among the biomaterial researchers is the recent development of biodegradable implants [1]. Implants for biomedical applications are used in different parts of the human body and remain in the body to avoid challenges and issues concerning their removal procedure. These adverse repercussions could be eliminated using biodegradable materials, which are dissolved and absorbed in the human body after the healing process is complete [1,2]. The existence of permanent implants such as stainless steel, titanium alloys and cobalt chromium alloys in the human body can cause allergic reactions and sensitization [3]. Polymer based material such as polyL-lactic acid have been employed as biodegradable implants but, these materials suffer from low mechanical strength, thereby limiting their application [2]. As a biodegradable material, Mg and its alloys can provide biocompatibility for orthopedic applications, particularly as a temporary stent [4]. Mg is also a fundamental element to the human body which is involved in many metabolic functions as it naturally exists in bone tissue [5]. However, the application of these materials has been limited due to high corrosion rate in physiological conditions and their fast biodegradation before the new tissue has adequately been healed [6]. In addition due to the relatively low mechanical strength of magnesium, it may not be suitable in load bearing applications. Hence, one of the main approaches for magnesium as a biodegradable implants is to improve the implants strength, elongation and corrosion resistance [7–9]. Alloying is one of the main tools to enhance the corrosion resistance of Mg alloy [4]. Aluminium-containing magnesium alloys improve the mechanical properties and corrosion resistance of pure Mg. However aluminium (Al) could cause nerve toxicity and Al^{3+} ion can

* Corresponding author. Address: No. 601, U3A, Kolej Perdana, UTM, Skudai 81310, Johor, Malaysia. Tel.: +60 147382258; fax: +60 75534610.
E-mail addresses: Rezabakhsheshi@gmail.com, Bhamidreza2@live.utm.my (H.R. Bakhsheshi-Rad).

also mix with inorganic phosphates causing its decline in the human body [10–12]. Elevated concentrations of Al^{3+} in the brain are related to Alzheimer's disease and can cause muscle fiber damage. Other alloying elements such as zirconium (Zr) may lead to lung cancer, liver cancer, nasopharyngeal cancer and breast cancer [5]. The addition of neodymium (Nd) and yttria (Y) into WE43 result in a disturbance at the implantation site [13]. However, in order to reduce the toxic effect of alloying elements, the utilization of elements which exist in the human body and which can retard the biodegradation of magnesium alloys are promising candidates for this approach. Zinc is a crucial element for the human body and it is necessary for many biological functions [4]. From materials viewpoint, Zn is known to increase age hardening response as it produces intermetallic compounds and refine the grain size [14,15]. A small amount of Zn contributes to the strength due to solid solution and precipitation strengthening [16,17]. Since zinc is more anodic to Fe and Ni that might be present as impurities in Mg alloys, it helps to overcome their harmful corrosion effect [18]. Calcium is the main composition of human bone and hence improved bone healing [16]. Manganese has the function of refining the grain size and improving tensile strength of magnesium alloys [19,20]. Khan et al. [21] reported that the grain size of AZ31 and AZ10 decreased with increasing Mn content and attained a constant grain size at Mn contents higher than 0.4 wt.%. However, it was also reported that addition of Mn has a grain refining effect on as-extruded Mg alloy [22]. Mn also decreases the corrosion rate of Mg via transforming iron and other metal elements to the harmless intermetallic compounds. It also plays an important role in the metabolic cycle of e.g. amino acids and carbohydrates [23,24]. Zhang et al. [24] reported that the addition of Mn and Zn into the magnesium alloy improved tensile strength and elongation. Sun et al. [4] showed that the addition of Zn and Ca into Mg matrix could enhance the corrosion potential and reduce the degradation rate. However, combinations of Mn and Zn into Mg–Ca alloys remain largely unstudied. Therefore, the main approach of this work is to investigate the microstructure, mechanical properties and corrosion behaviour of Mg–Ca–Mn–Zn alloy in comparison with that of the Mg–Ca alloy to reveal the effect of Mn and Zn on the mechanical and corrosion properties.

2. Experimental details

Magnesium alloys were prepared by melting 99.9% pure magnesium ingots, pure zinc chips (99.9%), Mg–4%Mn and Mg–32%Ca master alloy. The materials were melted by electrical resistance furnace under the protection of argon gas in a mild steel crucible coated with boron nitride at 760 °C. The molten metal was maintained for around 45 min at the melting condition for stabilization. After stabilizing, molten metal with different Zn (2, 4 and 7 wt.%) contents and a constant content of 0.5 Mn and 2 Ca wt.% were poured into mild steel moulds which had been preheated at 400 °C accompanied with 30 s stirring process. The chemical compositions of the binary Mg–Ca and Mg–Ca–Mn–Zn alloys are listed in Table 1. Specimens of 15 mm × 15 mm × 10 mm were cut from the achieved alloys ingots, and the samples were then mechani-

cally wet ground with 320–4000 silicon carbide (SiC) grit papers. Microstructure observation was performed using an optical microscope (Olympus BX60F5) and a scanning electron microscope (JEOL JSM-6380LA) equipped with EDS analysis. The grain size was measured based on the linear intercept method according to ASTM: E112-12 (2013). X-ray diffractometry (Siemens-D500) was used to evaluate phases present in the specimens by using Cu Kα line generated at 40 kV and 35 mA. Microhardness value of the samples was measured by Vickers hardness tester (Shimadzu) with 5 kg force. Tensile tests were performed by using an Instron-5569 universal testing machine at a displacement rate of 2.0 mm/min at ambient temperature. Specimens with a diameter of 6 mm and a gauge length of 30 mm were machined for tensile test. For each testing material, two specimens were examined. For compression test, cylindrical specimens with a diameter of 10 mm and a height of 20 mm were immersed in SBF for 10 days, and then cleaned in a boiling solution of chromium trioxide (CrO_3) to remove the surface corrosion product. The specimens were then dried in warm air.

Several rectangular specimens with a surface area of 1 cm^2 were molded in epoxy resin for electrochemical tests. The test was conducted at 37 °C in an open air glass cell containing 350 ml Kokubo solution at pH 7.66 by using PARSTAT 2263 potentiostat/galvanostat (Princeton Applied Research). A three-electrode cell was used for potentiodynamic polarization tests, where the reference electrode was saturated calomel electrode (SCE), the counter electrode was made of graphite rod, and the specimen was the working electrode. All experiments were carried out at a constant scan rate of 0.5 mV/s initiated at −250 mV below the open-circuit potential. To investigate the corrosion behaviour in vitro conditions, 15 mm × 20 mm × 5 mm samples were cut and mechanically ground by 320–2000 grit SiC sand paper. Afterward the ground samples were washed with distilled water, rinsed and degreased ultrasonically with ethanol, then dried at room temperature for immersion test. The specimens were then immersed in a beaker containing 200 ml of Kokubo simulated body fluid (SBF) with a chemical composition as listed in Table 2. The average pH value of the SBF from three measurements was recorded during the soaking experiment after an interval of 12 h. After the immersion test, the surface appearance of corroded specimens was assessed by using SEM and EDS. The hydrogen evolution rate of the specimens was also measured for 240 h in Kokubo solution. Two specimens with a similar condition were immersed in a beaker where a funnel was located over the samples to collect evolved hydrogen in a burette above the funnel. The hydrogen evolution rate was calculated in ml/cm^2/day before renewing the solution.

3. Results and discussion

3.1. Microstructure characterization

The optical micrographs of Mg–Ca and Mg–Ca–Mn–Zn alloys are shown in Fig. 1. As can be seen, the Mg–2Ca and Mg–4Ca alloys have average grain sizes of around 135 and 92 μm, respectively (Fig. 1a and b). It can also be observed that the amount of the secondary phases increased with the increases of the Ca content in the binary alloy. However, the addition of 0.5 wt.% Mn and 2 wt.% Zn

Table 1
Chemical compositions of the pure Mg, Mg–xCa and Mg–2Ca–0.5Mn–xZn alloys.

Alloy	Analysed compositions (wt.%)						
	Si	Mn	Zn	Ca	Al	Fe	Mg
Pure Mg	0.039	–	–	–	0.029	0.010	Bal.
Mg–2Ca	0.027	–	–	2.211	0.019	0.009	Bal.
Mg–4Ca	0.033	–	–	4.015	0.029	0.007	Bal.
Mg–2Ca–0.5Mn–2Zn	0.028	0.551	2.354	2.213	0.023	0.008	Bal.
Mg–2Ca–0.5Mn–4Zn	0.037	0.542	4.145	2.176	0.018	0.010	Bal.
Mg–2Ca–0.5Mn–7Zn	0.031	0.522	7.556	2.323	0.027	0.009	Bal.

Table 2
Chemical composition of the Kokubo simulated body fluid (SBF) compared to the human blood plasma.

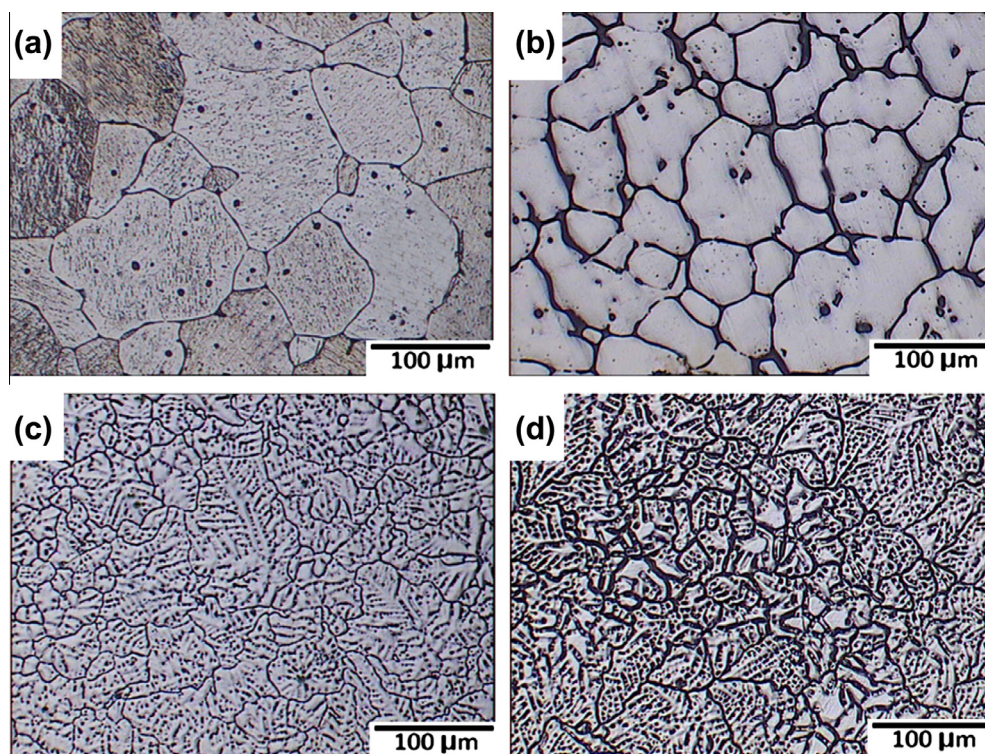| Solution	Ion concentration (mmol/L)							
	Na^+	K^+	Ca^{2+}	Mg^{2+}	HCO_3^-	Cl^-	HPO_4^{2-}	SO_4^{2-}
Plasma	142.0	5.0	2.5	1.5	27.0	103.0	1.0	0.5
Kokubo (c–SBF)	142.0	5.0	2.5	1.5	4.2	147.8	1.0	0.5

Fig. 1. Optical microscopic image of specimens (a) Mg–2Ca, (b) Mg–4Ca, (c) Mg–0.5Ca–0.5Mn–Zn alloys with different Zn content: 2 and (d) 4 wt.%.

resulted in further decrease in grain size to 78 μm (Fig. 1c). As the Zn content increased up to 4 wt.%, the grain size decreased significantly to 59 μm for Mg–2Ca–0.5Mn–4Zn alloy (Fig. 1d). These observations indicate that Zn can significantly refine the microstructure of Mg–Ca–Mn–Zn alloy. This phenomenon can be attributed to the formation of constitutional undercooling in a diffusion layer ahead of the solid/liquid interface as a result of the rejection of alloying elements at the front of grain growth which limits the growth stage, hence decreasing the grain size [25]. In terms of grain refinement, the growth restricted factor (Q), has a major role of alloying elements (solute) in controlling the grain size. Q is defined as $Q = mco\,(k–1)$, where m is the gradient of the liquidus line of a binary alloy, co is the bulk concentration of the solute and k is the equilibrium partition coefficient of the solute. A solute with a higher value of Q is expected to have a higher grain refining potency due to its stronger constitutional undercooling effect [26]. Mg–Zn system has a larger slope of the liquidus line, $m = 6.04$ °C/wt.%, compared to Mg–Ca ($m = 2.12$ °C/wt.%) which indicates a higher potential for Zn to reduce the grain size. Therefore, the growth restriction factor increases when Zn is added to the Mg–2Ca–0.5Mn–Zn alloy. The SEM observation of the sample is illustrated in Fig. 2b, which shows that the microstructure of binary Mg–Ca consisted of α-Mg and Mg_2Ca secondary phases. However, Mg–4Ca alloy showed a higher amount of Mg_2Ca phases in grain boundaries compared to Mg–2Ca alloy (Fig. 2c). In this case, the eutectic phases (α-Mg + Mg_2Ca) are formed within the grain boundary, and the width of the grain boundary becomes thicker as Ca content increases. The corresponding EDS analysis suggested that the light area which is composed of Mg and Ca, is related to the evolution of Mg_2Ca phase. Since the atomic ratio of Zn/Ca was less than 1.25, the addition of Mn and Zn into the binary Mg–2Ca alloy lead to the formation of Mg_2Ca and $Ca_2Mg_6Zn_3$ intermetallic phases (Fig. 2d). In Mg–2Ca–0.5Mn–2Zn alloy the lamellar eutectic (α-Mg + $Ca_2Mg_6Zn_3$ + Mg_2Ca) appeared along the grain boundary and its tri-pole junction. Similar types of phases are detected in the quaternary alloy contain 4 wt.% Zn but with different amounts

(Fig. 2e). Where the atomic ratio of Zn/Ca was more than that of 1.25, further addition to 7 wt.% Zn into the quaternary alloy resulted in the disappearance of Mg_2Ca intermetallic phase. The lamellar eutectic is composed of α-Mg, $Ca_2Mg_6Zn_3$ and $Mg_{12}Zn_{13}$ in the grain boundary accompanied by trace Mn (Fig. 2f). Fig. 3 shows the XRD pattern of as-cast samples of the Mg–Ca and Mg–Ca–Mn–Zn alloys. Apart from defined Mg reflections, the reflection of Mg_2Ca intermetallic phase appeared in Mg–2Ca and Mg–4Ca alloys. The XRD pattern of Mg–Ca binary alloy shows the presence of relatively small, although discernible, reflections of Mg_2Ca phases accompanied with Mg reflection. By addition of 0.5 wt.% Mn and 2 wt.% Zn the low intensity $Ca_2Mg_6Zn_3$ phase was detected in addition to Mg_2Ca and Mg phase reflections. The XRD pattern of Mg–2Ca–0.5Mn–4Zn alloy showed similar peaks. Diffraction peaks from the Mg_2Ca phase was not observed when Zn content was 7 wt.%. Due to the formation of trace amount of $Mg_{12}Zn_{13}$ and Mn which were beyond the detection limit of the XRD spectrum, these phases were not detected. The result of XRD analysis was further confirmed by the Mg–Ca–Mn–Zn phase diagram shown in Fig. 4a. As can be seen from this figure when 2 wt.% Zn is added, the alloy contains Mg_2Ca and $Ca_2Mg_6Zn_3$ compounds. In this case, a 100 g of the overall material, at room temperature, is composed of 93.1 g Mg, 2.6 g Mg_2Ca and 4.3 g $Ca_2Mg_6Zn_3$ (Fig. 4b). Similar types of phases are observed in the Mg–2Ca–0.5Mn–4Zn alloy but with different relative amounts as can be seen in Fig. 4c. 100 g of this alloy has only 0.8 g Mg_2Ca and 8.6 g $Ca_2Mg_6Zn_3$ at room temperature. However when 7 wt.% Zn is added, Mg_2Ca does not form hence a 100 g of the alloy consists of 86.5 g Mg, 10.5 g $Ca_2Mg_6Zn_3$ and 2.5 g $Mg_{12}Zn_{13}$ in addition to traces of Mn (Fig. 4d).

3.2. Mechanical properties

The mechanical properties of the binary Mg–Ca alloys in comparison with quaternary Mg–Ca–Mn–Zn alloys are summarized in Table 3. The ultimate tensile strength (UTS) and elongation of as-cast pure magnesium were 97.5 MPa and 7.31%, respectively
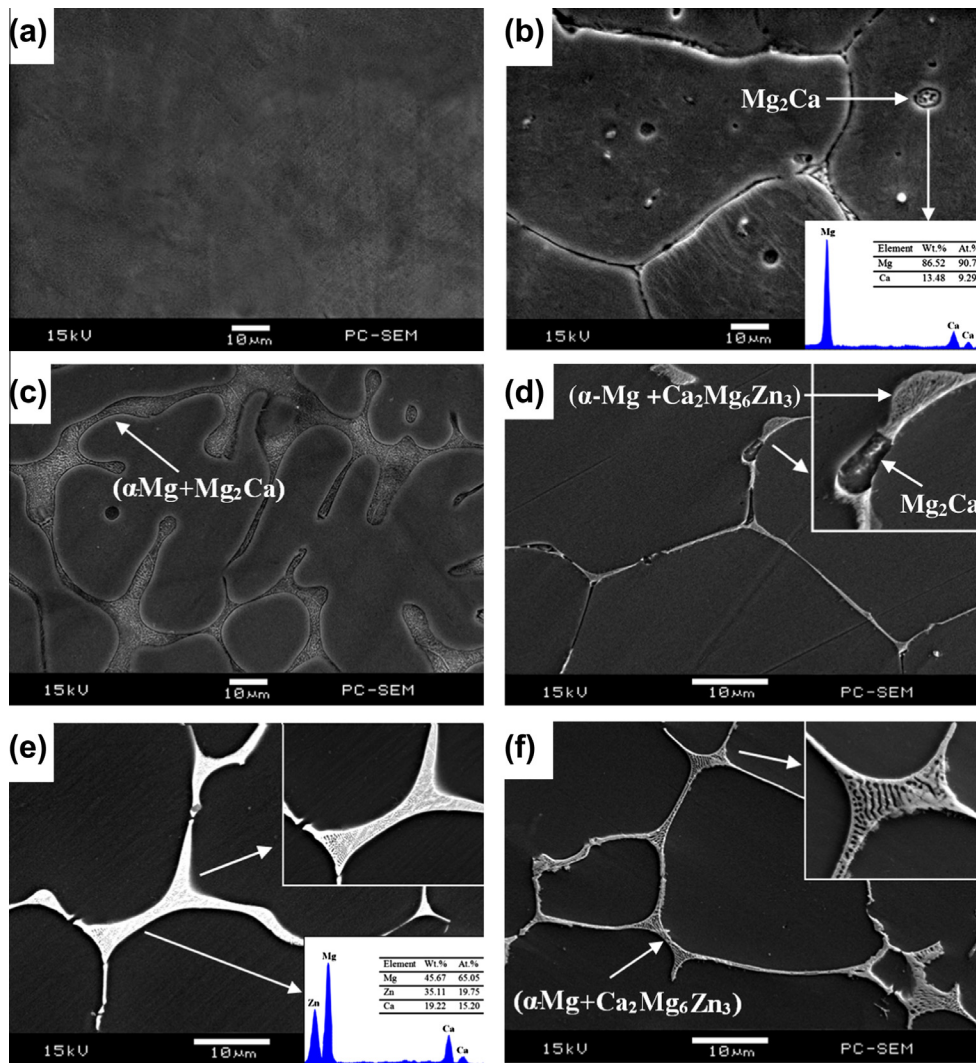
Fig. 2. SEM micrographs of (a) pure Mg (b) Mg–2Ca, (c) Mg–4Ca, (d) Mg–0.5Ca–0.5Mn–Zn alloys with various Zn content: 2 (e) 4 and (f) 7 wt.%.
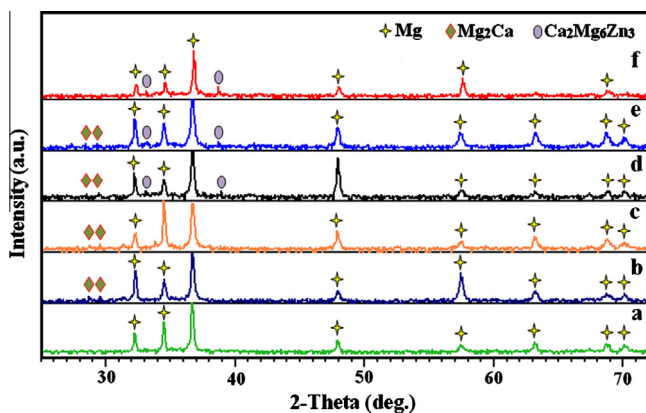

Fig. 3. X-ray diffraction patterns of (a) pure Mg (b) Mg–2Ca, (c) Mg–4Ca, (d) Mg–0.5Ca–0.5Mn–Zn alloys with various Zn content: 2 (e) 4 and (f) 7 wt.%.

(Fig. 5). However, after the addition of 2 wt.% Ca into the binary Mg–Ca alloy the UTS increased to the 115.2 MPa but, the elongation decreased to 3.05%. The Mg$_2$Ca phase leads to a decrease in the ductility as this phase distributed at the grain boundary and can act as crack source for the Mg–Ca alloy [27]. The UTS and elongation declined dramatically to 125.4 MPa and 2.10% respectively, when 4 wt.% Ca was introduced to the binary alloy. Compared to binary Mg–Ca alloy, the UTS, and elongation of quaternary Mg–Ca–Mn–Zn alloys increased with increases in Zn content up to 4 wt.%. Its UTS and elongation were 189.2 MPa and 8.71%, respectively. The enhancement of UTS is due to the grain refining and solution strength effects and second phase strengthening. Conversely, Mg–2Ca–0.5Mn–7Zn alloy exhibits deteriorated tensile properties. The UTS of the aforesaid alloy decreased to 140.7 MPa, and elongation also declined to 4.15%. Formation of network structure of the second phase at the grain boundary which could act as crack source is the main reason for the decrease in UTS and elongation [28]. The hardness value of pure Mg was 28.9 Hv and this value increased to 43.2 and 53.3 Hv with increasing Ca content for Mg–2Ca and Mg–4Ca alloy respectively. This can be attributed to precipitation of the Mg$_2$Ca phase within the α-Mg matrix and the grain boundary. However, in quaternary alloy the addition of 2 wt.% Zn into the binary Mg–2Ca–0.5Mn alloy caused an increased in the hardness value to 64.5 Hv. As discussed above, the maximum solubility of Zn in the Mg–Zn alloys is 1.6 wt.% at ambient temperature at equilibrium [29]. Beyond this value Mg$_2$Ca and Ca$_2$Mg$_6$Zn$_3$ phases started to precipitate within the α-Mg matrix and the grain boundaries, which was the main reason for the enhanced in hardness. Further additions of Zn to 4 wt.% into the
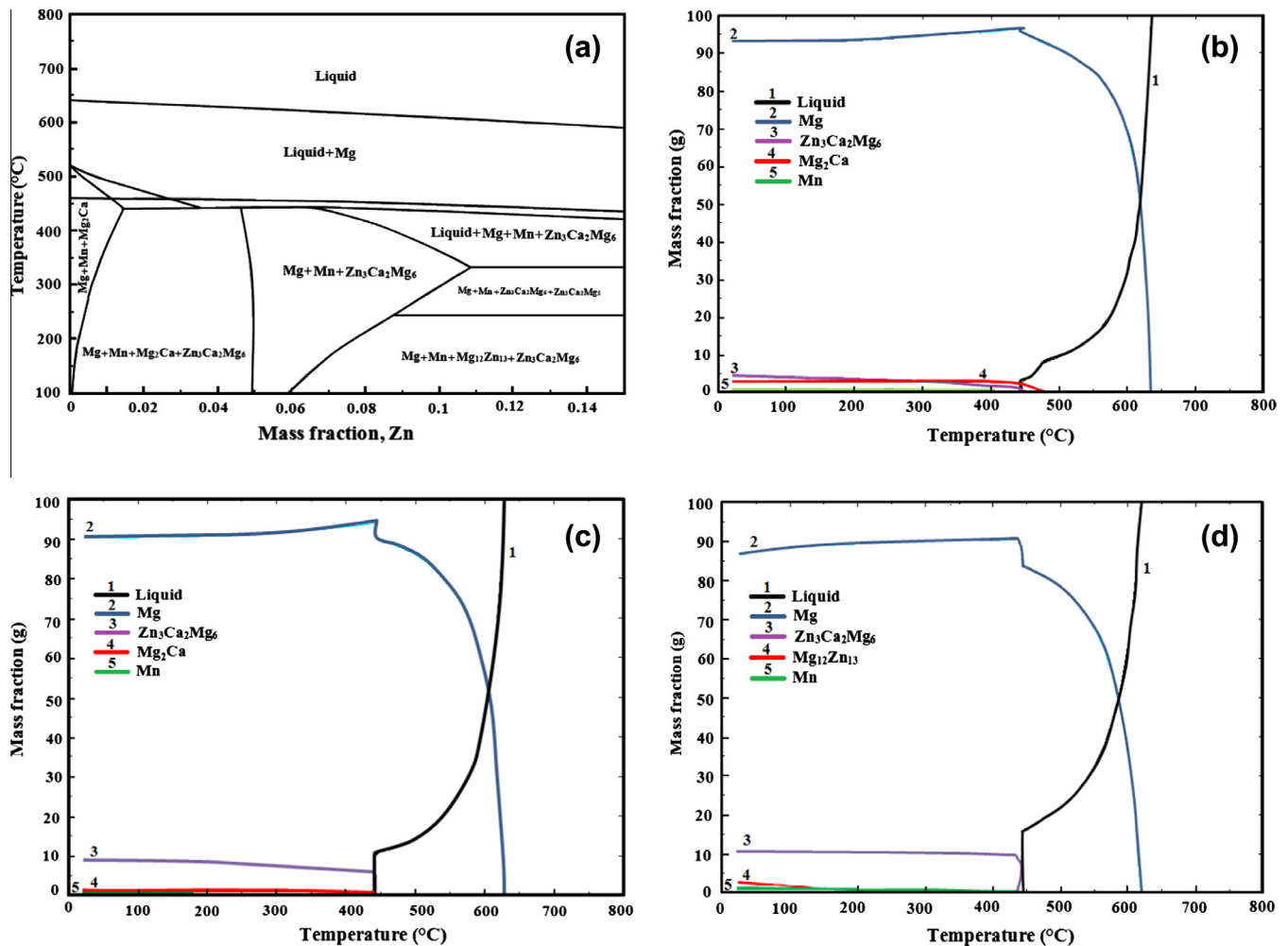
Fig. 4. (a) Calculated phase fraction vs. temperature for Mg–2Ca–0.5Mn–xZn and phase assemblage diagram of (b) Mg–2Ca–0.5Mn–2Zn, (c) Mg–2Ca–0.5Mn–4Zn and (d) Mg–2Ca–0.5Mn–7Zn.

Table 3
Mechanical properties of the as-cast binary Mg–Ca and quaternary Mg–Ca–Mn–Zn alloys.

Specimen	Yield strength (MPa)	Tensile strength (MPa)	Elongation (%)	Hardness (Hv)
Pure Mg	27.5	97.5	7.31	28.9
Mg–2Ca	47.3	115.2	3.05	43.2
Mg–4Ca	34.5	77.4	2.10	53.3
Mg–2Ca–0.5Mn–2Zn	78.3	168.5	7.84	64.5
Mg–2Ca–0.5Mn–4Zn	83.1	189.2	8.71	69.1
Mg–2Ca–0.5Mn–7Zn	45.4	140.7	4.15	82.2

quaternary alloy lead to an increase in hardness to 69.1 Hv due to more precipitates in the Mg$_2$Ca and Ca$_2$Mg$_6$Zn$_3$ phases. These precipitates act as obstacles to grain boundary sliding, thus restricting further grain growth. When the content of Zn reached up to 7 wt.% the hardness value increased to 82.2 Hv due to the further refining effect of Zn on the alloys. In addition, precipitation of Mg$_{12}$Zn$_{13}$ and Ca$_2$Mg$_6$Zn$_3$ phases along the grain boundaries were other factors causing an increase in hardness value.

Table 4 exhibits the compression strength of the binary Mg–Ca and quaternary Mg–Mn–Ca–Zn alloys before and after immersion in SBF for duration of 10 days. The compression strength of

pure Mg before immersion was 185.4 MPa and this value decreased by 19% after immersion in SBF. The compression strength of the binary Mg–2Ca and Mg–4Ca alloys decreased to 197.6 and 174.4 MPa after immersion for 10 days, respectively. Apparently, the addition of 2 and 4 wt.% Zn into the quaternary Mg–Ca–Mn–Zn alloy resulted in the compression strength of the specimen before immersion increasing to 336.1 and 343.6 MPa. However, these values after immersion decreased to 315.6 and 305.2 MPa, respectively which is comparable to the compressive strength of human bones (100–230 MPa) in cortical bone. This phenomenon showed that the addition of Mn and Zn to the alloy leads to delay the loss of the mechanical property of the binary Mg–Ca alloy. The compressive strength of the quaternary alloy decreased to 299.2 MPa after immersion when 7 wt.% Zn was added to alloy. This is because the Mg–2Ca–0.5Mn–7Zn alloy shows higher degradation rates compared to the other quaternary alloys. The Mg–2Ca–0.5Mn–2Zn showed the highest compressive strength after immersion. This was due to the uniform distribution of Ca$_2$Mg$_6$Zn$_3$ and Mg$_2$Ca along the grain boundaries which acted as obstacles for electron transfer from α-Mg phase to another phase. This phenomenon led to further electron transfer resistance between α-Mg phase and the intermetallic phases. This resulted in the reduction of the effective driving force for galvanic corrosion causing a decline in the corrosion reaction thus reducing the degradation rate [30].
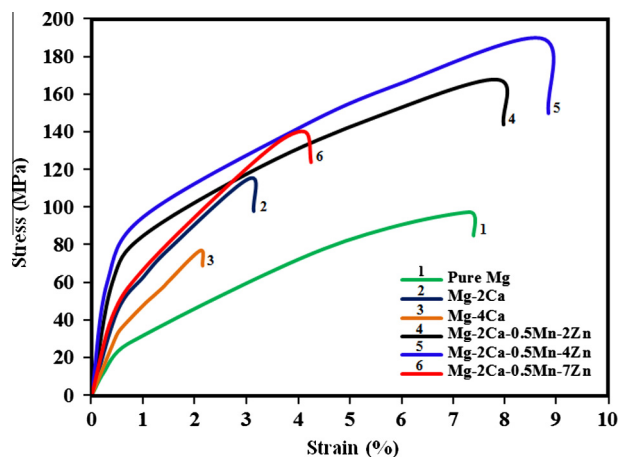
Fig. 5. Typical stress–strain curve of as-cast pure Mg, Mg–Ca and Mg–Ca–Mn–Zn alloys.

Table 4
Compression test results of the pure Mg, Mg–Ca and Mg–Ca–Mn–Zn alloys before and after immersion in SBF.

Specimen	Compression strength (MPa) before immersion	Compression strength (MPa) after immersion
Pure Mg	185.4	149.2
Mg-2Ca	235.7	197.4
Mg-4Ca	250.7	174.4
Mg-2Ca–0.5Mn–2Zn	336.1	315.6
Mg-2Ca–0.5Mn–4Zn	343.6	305.2
Mg-2Ca–0.5Mn–7Zn	362.8	299.2

3.3. Electrochemical measurements

Fig. 6 shows polarization curves of Mg–Ca–Mn–Zn alloys in comparison with Mg–Ca alloys. The corrosion potential of Mg–2Ca alloy was −1996.8 mV$_{SCE}$ which was relatively about 30.6 mV$_{SCE}$ and 57.7 mV$_{SCE}$ lower than that of the pure Mg and Mg–4Ca alloy respectively. The curves also show that Mg–2Ca and Mg–4Ca alloys have more negative potential compared to the quaternary Mg–2Ca–0.5Mn–2Zn alloy indicating that Mn and Zn have a significant effect on the corrosion behaviour of the alloy. By addition of 0.5 wt.% Mn and 2 wt.% Zn into the binary Mg–2Ca alloy, the corrosion potential shifted towards significant nobler direction. The corrosion current density of the Mg–2Ca–0.5Mn–2Zn alloy was 1.78 μA/cm^2, lower than the Mg–2Ca (301.9 μA/cm^2) and Mg–4Ca (395.7 μA/cm^2), indicating that the intermetallic phase has a considerable effect on the corrosion rate of the alloy. In general, cathodic polarization curves were assumed to indicate hydrogen evolution via water reduction, however the anodic polarization curves exhibited the dissolution of Mg [31]. The kinetic of cathodic reaction in pure Mg, Mg–2Ca and Mg–4Ca alloys are faster compared with Mg–2Ca–0.5Mn–2Zn alloy. This phenomenon indicates that the cathodic reaction was kinetically more difficult in the quaternary alloys compared to the binary one. Addition of 0.5 Mn and 4 wt.% Zn into the binary Mg–2Ca alloys lead to a shift in the corrosion potential toward a more positive direction (−1652.2 mV$_{SCE}$) and decreased corrosion current density to (99.6 μA/cm^2). However, when 7 wt.% Zn was introduced to the alloy the corrosion potential moved toward a negative direction (−1728.3 mV$_{SCE}$) while corrosion current increased to 174.1 μA/cm^2.

A plateau was also observed in the polarization curves of quaternary alloy which show a passive film formed on the surface of Mg–Ca–Mn–Zn alloy when the sample was immersed in SBF. How-
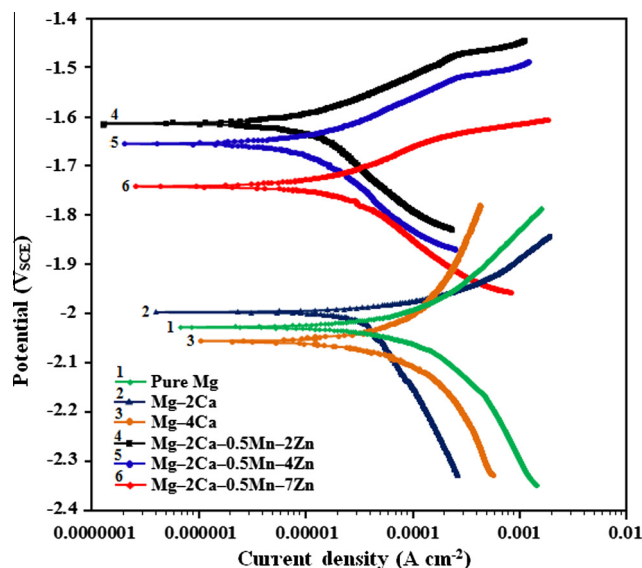

Fig. 6. Potentiodynamic polarization curves of pure Mg, Mg–Ca and Mg–Ca–Mn–Zn alloys specimens in Kokubo solution.

ever, there is no passivation stage in the curve of binary Mg–Ca alloys which means that the addition of Mn and Zn reduce the cathodic current density and decrease the rate of hydrogen evolution. In quaternary alloys the breaking potential (E_b) of 2 wt.% Zn containing alloys is more positive than that of 4 and 7 wt.% Zn containing alloy. Therefore, the localized corrosion is less likely to occur in the Mg–2Ca–0.5Mn–2Zn alloy than other alloys [27]. The high corrosion potential accompanied by high breaking potential and low corrosion current obviously describe a lower corrosion rate of the quaternary Mg–Ca–Mn–Zn alloy compared to the binary Mg–Ca alloys. The corrosion current density (i_{corr}), corrosion potential (E_{corr}, V$_{SCE}$), cathodic Tefal slops (β_c), anodic Tefal slopes (β_a) and corresponding corrosion rate (P_i) of specimens extracted from the polarization curves are shown in Table 5. The corrosion current density, i_{corr} (μA/cm^2), is related to the corrosion rate, P_i with using the following equation: [32].

$$P_i = 22.85 i_{corr} \tag{1}$$

In addition to the electrochemical parameters (i_{corr}, β_a and β_c) of specimens the polarization resistance (R_P) was calculated according following equation: [33].

$$R_P = \frac{\beta_a \beta_c}{2.3(\beta_a + \beta_c) i_{corr}} \tag{2}$$

The addition of 2 wt.% of Ca into the pure Mg alloy leads the R_P to increase from 0.82 kΩ cm^2 to 0.95 kΩ cm^2. However, further addition of Ca to 4% into the binary Mg–Ca alloy decreased R_P value to 0.78 kΩ cm^2. In contrast, the addition of Zn to 2 and 4 wt.% into the binary alloy improve R_P value to 3.26 and 2.38 kΩ cm^2 while, more increasing Zn to 7 wt.% saw the the R_P value decline to 1.44 kΩ cm^2. In binary Mg–Ca alloy the formation of galvanic couple between the Mg$_2$Ca phase and Mg matrix decreased the corrosion resistance of the alloy [34]. In the galvanic couple of Mg–Ca alloy, the Mg$_2$Ca phase is assumed as the cathode while, the α-Mg phase is the anode. It can also be seen that with increasing calcium content the corrosion potential becomes more negative followed by an increase in corrosion rate. This is due to the high electrochemical activity of Mg$_2$Ca compared to the α-Mg [35]. Quaternary Mg–2Ca–0.5Mn–2Zn and Mg–2Ca–0.5Mn–4Zn alloys are composed of α-Mg, Mg$_2$Ca and Ca$_2$Mg$_6$Zn$_3$ phases in which the Ca$_2$Mg$_6$Zn$_3$ phase acts as cathode and the Mg$_2$Ca phase acts as the

Table 5
Electrochemical parameters of pure Mg, Mg–Ca and Mg–Ca–Mn–Zn specimens in Kokubo solution attained from the polarization test.

Alloy	Corrosion potential, E_{corr} (mV vs. SCE)	Current density, i_{corr} (μA/cm^2)	Cathodic slope, β_C (mV/decade) vs. SCE	Anodic slope, β_a (mV/decade) vs. SCE	Polarization resistance, R_P (kΩ cm^2)	Corrosion rate, P_i (mm/year)
Pure Mg	−2027.4	370.7	221.7	105.2	0.82	8.47
Mg–2Ca	−1996.8	301.9	218.3	94.6	0.95	6.89
Mg–4Ca	−2054.5	395.7	227.6	104.3	0.78	9.04
Mg–2Ca–0.5Mn–2Zn	−1616.6	78.3	111.1	125.1	3.26	1.78
Mg–2Ca–0.5Mn–4Zn	−1652.2	99.6	107.7	110.5	2.38	2.27
Mg–2Ca–0.5Mn–7Zn	−1728.3	174.1	82.2	195.2	1.44	3.98

anode. It can be concluded that Mg$_2$Ca phase was more reactive (corroded faster) than the Ca$_2$Mg$_6$Zn$_3$ and α-Mg phases while, the Ca$_2$Mg$_6$Zn$_3$ phase was less active than α-Mg [27]. It was suggested that Mg$_2$Ca plays an important role in the improvement in the corrosion resistance of Mg–Ca–Mn–Zn when the Zn/Ca ratio was less than 1.25. Further addition of Zn to 7 wt.% resulted in the disappearance of Mg$_2$Ca phase, hence in Mg–0.5Mn–2Ca–7Zn alloys the galvanic couple occurred between Ca$_2$Mg$_6$Zn$_3$ and Mg$_{12}$Zn$_{13}$ phases where Ca$_2$Mg$_6$Zn$_3$ phase is cathode and Mg$_{12}$Zn$_{13}$ phase is anode. In this condition after immersion, the Ca$_2$Mg$_6$Zn$_3$ phase remained in the structure while Mg$_{12}$Zn$_{13}$ and α-Mg phase were corroded and almost disappeared. Therefore α-Mg cannot further support of the Ca$_2$Mg$_6$Zn$_3$ phase and corrosion resistance decreased.

3.4. Immersion test

The pH variation of the SBF for Mg–Ca and Mg–Ca–Mn–Zn alloys as a function of immersion time is shown in Fig. 7. From the graph it can be seen that the pH values of the pure Mg increased from about 7.66 to 8.62 during early immersion stages. Similar trends are observed for the binary and quaternary alloys. Early increase in pH values for specimens was caused by the release of hydroxide (OH$^-$) ions into the solution [28]. Also it can be seen that Mg–4Ca and Mg–2Ca alloys can rapidly alkalize the SBF. However, the alkalization effect of the other alloys is relatively slow. Afterwards, the pH value of SBF increased with lower slop by immersion time due to the formation of magnesium hydroxide, Mg(OH)$_2$, and the precipitation of calcium phosphate on the surface of the alloy. In contrast, the pH values of the SBF corresponding to Mg–4Ca and pure Mg increased with higher slop and reached 10.45 and 10.05 respectively. It was reported that the attack of the chloride ions on Mg(OH)$_2$ would lead to an increase in interfacial pH > 10 [1]. However, the pH values of Mg–Ca–Mn–Zn alloys were lower than those of pure Mg and Mg–Ca alloys. The pitting corrosion of the pure Mg and Mg–Ca alloys generated more Mg^{2+} ions which lead to an increased in the pH values of specimens. Conversely, formation of the compact film layer on the surface of quaternary Mg–Ca–Mn–Zn alloys resulted in difficult contact between matrix and SBF significantly decreasing the corrosion reaction and subsequently pH values.

Fig. 8 shows corrosion morphologies of Mg–Ca and Mg–Ca–Mn–Zn alloys specimens after immersion in Kokubo solution for 144 h. Fig. 8a shows that the pure Mg surface is covered with many pits of different depths and sizes. Simultaneously some corrosion product started to form on the surface of the specimen particularly on the corroding area and some dropped off from the surface as immersion time increased. Fig. 8b revealed that cracks with heterogeneous distribution formed on the surface of Mg–2Ca alloy. The crack formation can be due to water loss of the corrosion products and surface shrinkage. The existence of cracks makes the solution contact with the matrix easier, accelerating the corrosion of the matrix. Further addition of Ca up to 4 wt.% leads to formation of a large number of deep corrosion pits on the surface of the Mg–
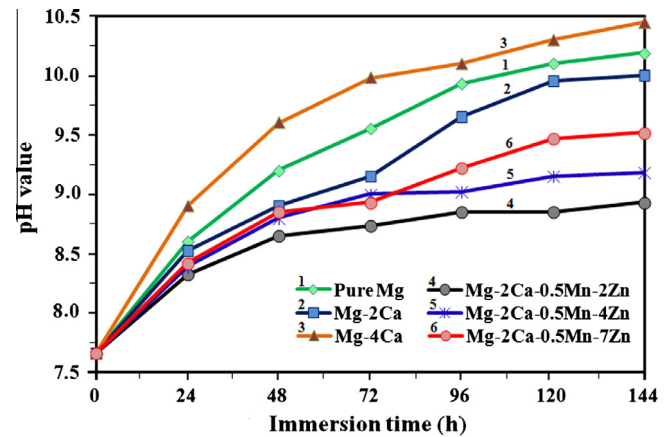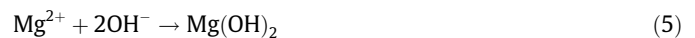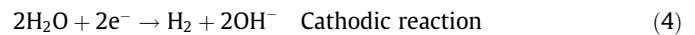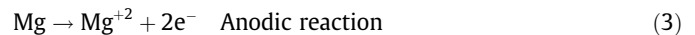

Fig. 7. Change in pH of the Kokubo solution during immersion of pure Mg, Mg–Ca and Mg–Ca–Mn–Zn specimens for duration of 144 h.

4Ca alloy (Fig. 8c). Magnesium dissolution and deposit layer formed according to the following reaction:

$$Mg \rightarrow Mg^{+2} + 2e^- \quad \text{Anodic reaction} \tag{3}$$

$$2H_2O + 2e^- \rightarrow H_2 + 2OH^- \quad \text{Cathodic reaction} \tag{4}$$

$$Mg^{2+} + 2OH^- \rightarrow Mg(OH)_2 \tag{5}$$

$$Mg(OH)_2 + Cl^- \rightarrow MgCl_2 + 2OH^- \tag{6}$$

The chloride ion (Cl$^-$) present in the Kokubo solution can easily penetrate the film and reacts with Mg(OH)$_2$ to produce the more soluble magnesium chloride (MgCl$_2$) [36], which then dissociates into Mg^{2+} and 2Cl$^-$ causing an increase in OH$^-$ ions near the surface of the sample. Mg(OH)$_2$ layer is loose and its dissolution makes the surface more active, subsequently decreasing the protected area and causing further dissolution of magnesium. In addition, generation of OH$^-$ ions obtained from the cathodic reaction increases the local pH of the solution stabilizing the Mg(OH)$_2$. Eventually phosphate PO$_4^{3-}$ and Ca^{2+} in the solution reacted with OH$^-$ to form hydroxyapatite (HA) [Ca$_{10}$(PO$_4$)$_6$(OH)$_2$], which tend to nucleate and grow on the surface of untreated specimens. However, Fig. 8d indicates that the surface of Mg–2Ca–0.5Mn–2Zn alloy is covered by insoluble corrosion film Mg(OH)$_2$ and small particles. It was reported that Mg(OH)$_2$ is insoluble in water, and the water-soluble part can be totally ionized, resulting in Mg^{2+} and OH$^-$ [37].

The presence of manganese in equilibrium with Mg solid solution matrix also has a beneficial influence on the corrosion behaviour of the Mg–Ca–Mn–Zn quaternary alloys. This can be attributed to the surface film covering Mn-containing magnesium alloys which contain a manganese oxide [17,20]. It is believed that incorporation of oxidized manganese in magnesium hydroxide through replacement of the magnesium cations to supress the penetration
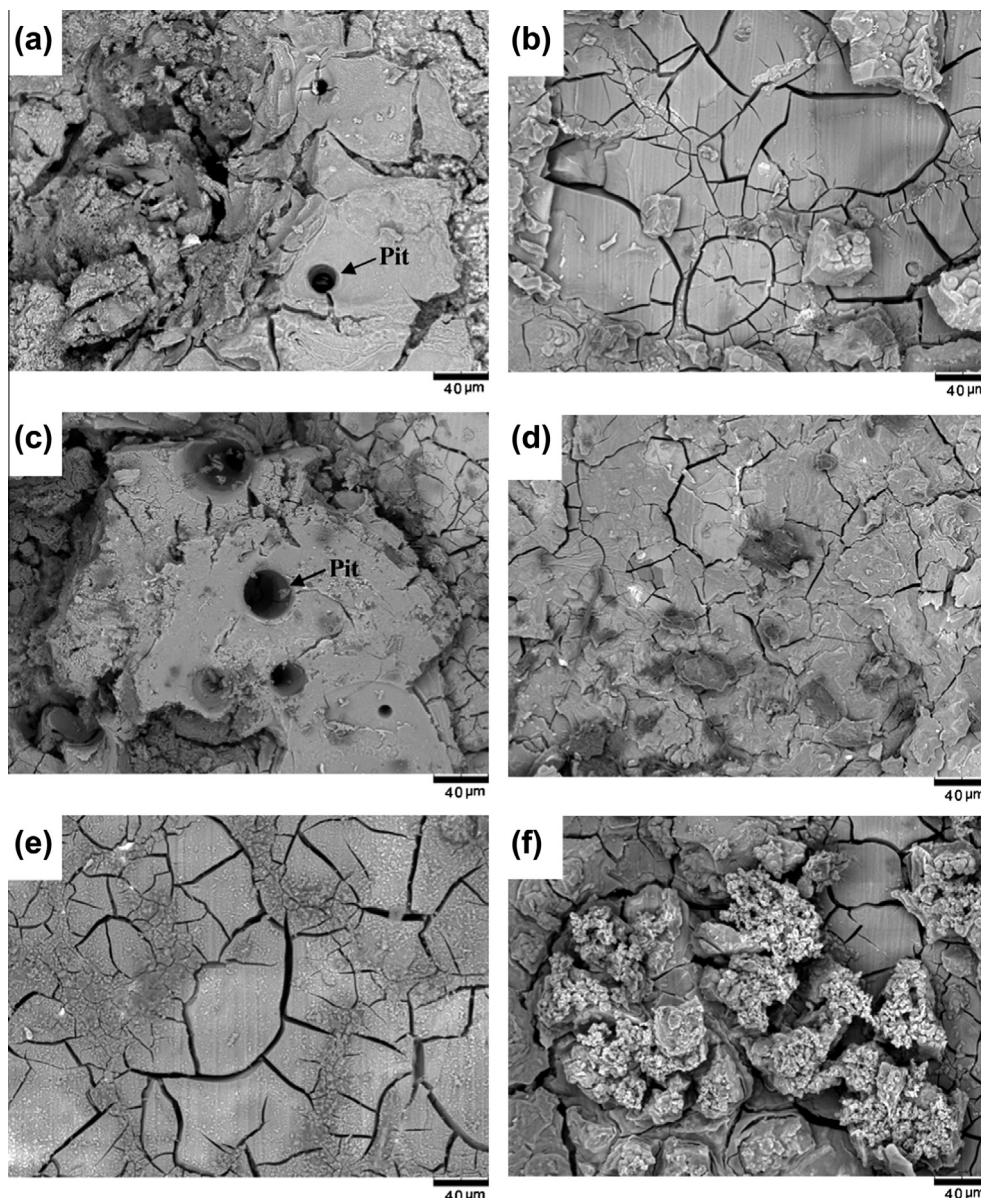
Fig. 8. SEM micrographs of (a) pure Mg (b) Mg–2Ca, (c) Mg–4Ca, (d) Mg–0.5Ca–0.5Mn–Zn alloys with various Zn content: 2 (e) 4 and (f) 7 wt.% after immersion into Kokubo for 144 h duration.

of chloride anions into the magnesium hydroxide which provides a good barrier to improve the corrosion resistance of the quaternary alloy. Further addition of Zn to 4 wt.% resulted in the formation of more deep cracks due to higher dehydration of the surface layer after removal of the specimen from the SBF (Fig. 8e). However, Mg–2Ca–0.5Mn–7Zn alloy suffers from heavy corrosion product by precipitation of non-uniformed big white particles on the crack layer (Fig. 8f).

The XRD pattern of binary Mg–Ca and quaternary Mg–Ca–Mn–Zn alloys (Fig. 9) shows the existence of $Mg(OH)_2$ peaks accompanied by peaks of Mg and HA. The Mg–4Ca alloy showed more broad $Mg(OH)_2$ peaks as main corrosion products than that of pure Mg and Mg–2Ca alloy. However by addition of 2 wt.% Zn into the binary alloy the diffraction intensities of HA phases increased. Furthermore it was observed that the diffraction intensities of $Mg(OH)_2$ phases increased in Mg–Ca–Mn–Zn alloys with increasing Zn content and the highest intensity of $Mg(OH)_2$ peaks were detected after the addition of more than 7 wt.% Zn content into

the quaternary alloy. It suggests that a considerable amount of $Mg(OH)_2$ was formed on the surface of specimens.

The FTIR spectrum of corrosion product of Mg–Ca and Mg–Ca–Mn–Zn alloys are shown in Fig. 10. It is obvious that the kinds of the corrosion products which formed on the surface of Mg–Ca and Mg–Ca–Mn–Zn alloys were similar but their amounts were different. The peak detected at $3709 \, cm^{-1}$ was related to the O–H stretching mode which confirms the formation of $Mg(OH)_2$. It was reported that $Mg(OH)_2$ has a hexagonal crystal structure which easily undergoes basal cleavage caused by the formation of crack on the corrosion product layer. Therefore, the formation of mud-patterns could be due to $Mg(OH)_2$ [1]. The band at $3464 \, cm^{-1}$ is also attributed to water vibration. It can be also be observed that the absorbance of the spectra from the $Mg(OH)_2$ was significantly higher in Mg–4Ca alloy compared to the other alloys. Phosphate groups (PO_4^{-3}) are detected at $1174 \, cm^{-1}$ and $1066 \, cm^{-1}$ for the P–O stretching v_1, while the detection of weak bands at $2887 \, cm^{-1}$ could be attributed to $H_2PO_4^{-2}$ ion. These
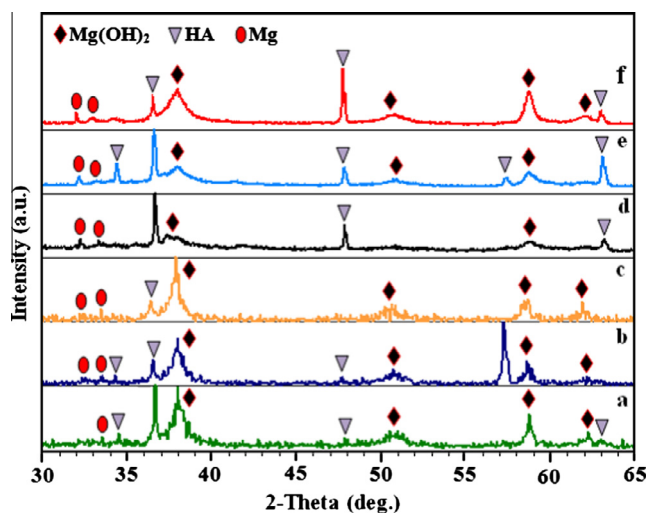
Fig. 9. X-ray diffraction patterns attained from the corrosion products of (a) pure Mg (b) Mg–2Ca, (c) Mg–4Ca, (d) Mg–0.5Ca–0.5Mn–Zn alloys with various Zn content: 2 (e) 4 and (f) 7 wt.% after full immersion exposure to SBF solution for 144 h duration.
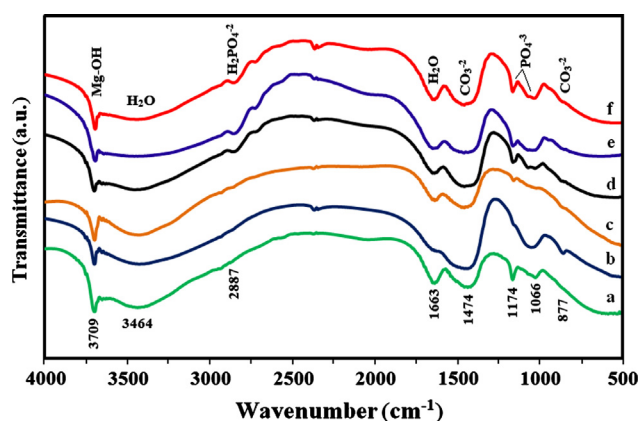

Fig. 11. Hydrogen evolution of the pure Mg, Mg–Ca and Mg–Ca–Mn–Zn specimens specimens immersed in Kokubo solution for duration of 240 h.

4. Conclusions

Microstructure observation indicated that by the addition of Mn and Zn elements into the binary Mg–Ca alloy the grain sizes are significantly refined and a large number of secondary phases precipitated in the grains. The mechanical and bio-corrosion properties of the binary Mg–Ca and quaternary Mg–Ca–Mn–Zn alloys are significantly affected by the type and amount of secondary phases. The mechanical properties of the binary Mg–Ca alloys decreased significantly by addition of 4 wt.% Ca. However, after the addition of Zn and Mn into the binary Mg–2Ca alloys the UTS and elongation can be enhanced by about 31.5% and 64.9% respectively. The compression tests showed that the addition of Zn and Mn also can delay the loss of the compressive integrities of the binary Mg–Ca alloys. Corrosion tests in Kokubo solution show that the addition of Mn and Zn into the binary alloy leads a shift in the corrosion potential towards more noble direction and hence decreased the degradation rate of the alloy. The surface of the corroded quaternary Mg–Ca–Mn–Zn alloy is smoother and contains lower amounts of pit than Mg–Ca alloys which is mainly associated with formation of eutectic (Mg + Mg_2Ca + $Ca_2Mg_6Zn_3$) phase. The protection performance of the $Mg(OH)_2$ in quaternary Mg–2Ca–0.5Mn–2Zn is better compared to the binary Mg–2Ca alloy owing to the incorporation of oxidized manganese into the magnesium hydroxide. Therefore, the Mg–2Ca–0.5Mn–2Zn with good strength and corrosion resistance is an interesting candidate for the development of biomedical applications.

Fig. 10. FTIR absorption spectra attained from the corrosion products of (a) pure Mg (b) Mg–2Ca, (c) Mg–4Ca, (d) Mg–0.5Ca–0.5Mn–Zn alloys with various Zn content: 2 (e) 4 and (f) 7 wt.% after full immersion exposure to SBF solution for 144 h duration.

P–O bands in the specimens as a consequence of the existence of HA, are more specific. The bands for the carbonate groups (887 cm^{-1}: C–O stretching v_4) are consistent with the spectra for apatite compositions. FTIR confirmed the formation of magnesium hydroxide and hydroxyapatite on the surface of specimens after being immersed in the Kokubo solution for 196 h duration. The FTIR results were in good agreement with the XRD results.

Fig. 11 shows the hydrogen evolution results of the binary and quaternary alloys in SBF for duration of 240 h. It can be seen that the hydrogen evolution rate of the alloys during the first 48 h is higher compared that the rate with the increase immersion duration. The binary Mg–2Ca alloy shows lower hydrogen evolution (42.3 ml/cm^2/day) compared to the pure Mg (56.5 ml/cm^2/day) and Mg–4Ca alloy (64.1 ml/cm^2/day). It was reported that subcutaneous gas pockets can occur due to the rapid evolution of hydrogen bubbles. This can cause postponement in healing in the surgical vicinity which leads to necrosis of tissues and possible discomfort [38]. However, by addition of 0.5 wt.% Mn and 2 wt.% Zn into the binary Mg–Ca alloy the hydrogen evolution significantly decreased to 16.1 ml/cm^2/day. Further addition of Zn to 4 and 7 wt.% Zn leads to increases in the hydrogen evolution volume to 28.5 and 38.4 ml/cm^2/day, suggesting that the corrosion resistance is decreased by increasing zinc content in quaternary alloys.

References
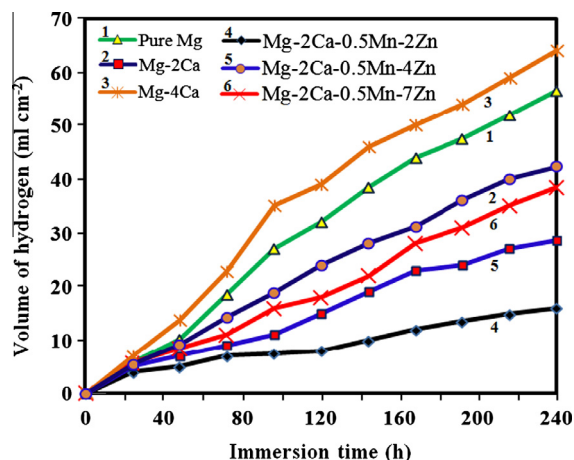
[1] Jamesh M, Kumar S, Sankara Narayanan TSN. Corrosion behavior of commercially pure Mg and ZM21 Mg alloy in Ringer's solution – Long term evaluation by EIS. Corros Sci 2011;53:645–54.
[2] Chiu KY, Wong MH, Cheng FT, Man HC. Characterization and corrosion studies of fluoride conversion coating on degradable Mg implants. Surf Coat Technol 2007;202:590–8.
[3] Shi Y, Qi M, Chen Y, Shi P. MAO-DCPD composite coating on Mg alloy for degradable implant applications. Mater Lett 2011;65:2201–4.
[4] Sun Y, Zhang B, Wang Y. Preparation and characterization of a new biomedical Mg–Zn–Ca alloy. Mater Des 2012;34:58–64.
[5] Song G. Control of biodegradation of biocompatable magnesium alloys. Corros Sci 2007;49:1696–701.
[6] Zhou P, Gong HR. Phase stability, mechanical property, and electronic structure of an Mg–Ca system. J Mech Behav Biomed 2012;8:154–64.
[7] He W, Zhang E, Yang K. Effect of Y on the bio-corrosion behavior of extruded Mg–Zn–Mn alloy in Hank's solution. Mater Sci Eng C 2010;30:167–74.
[8] Yang M, Liang X, Yi Z, Pan F. Effects of zirconium addition on as-cast microstructure and mechanical properties of Mg–3Sn–2Ca magnesium alloy. Mater Des 2011;32:1967–73.

[9] Jihua C, Juying W, Hongge Y, et al. Effects of cooling rate and pressure on microstructure and mechanical properties of sub-rapidly solidified Mg–Zn–Sn–Al–Ca alloy. Mater Des 2013;45:300–7.

[10] Zhang X, Wang Z, Yuan G, et al. Improvement of mechanical properties and corrosion resistance of biodegradable Mg–Nd–Zn–Zr alloys by double extrusion. Mater Sci Eng B 2012;177:1113–9.

[11] Gu XN, Li N, Zheng YF, et al. In vitro degradation performance and biological response of a Mg–Zn–Zr alloy. Mater Sci Eng B 2011;176:1778–84.

[12] Zhang W, Li M, Chen Q, Hu W. Effects of Sr and Sn on microstructure and corrosion resistance of Mg–Zr–Ca magnesium alloy for biomedical applications. Mater Des 2012;39:379–83.

[13] Zhang S, Li J, Song Y. In vitro degradation, hemolysis and MC3T3-E1 cell adhesion of biodegradable Mg–Zn alloy. Mater Sci Eng C 2009;29:1907–12.

[14] Li N, Zheng Y. Novel magnesium alloys developed for biomedical application: a review. J Mater Sci Technol 2013:1–14.

[15] Su Z, Liu C, Wan Y. Microstructures and mechanical properties of high performance Mg–4Y–2.4Nd–0.2Zn–0.4Zr alloy. Mater Des 2013;45:466–72.

[16] Li Z, Gu X, Lou S, et al. The development of binary Mg–Ca alloys for use as biodegradable materials within bone. Biomaterials 2008;29:1329–44.

[17] Rosalbino F, De Negri S, Scavino G, Saccone A. Microstructure and in vitro degradation performance of Mg–Zn–Mn alloys for biomedical application. J Biomed Mater Res A 2013;101:704–11.

[18] Zhang X, Yuan G, Mao L. Effects of extrusion and heat treatment on the mechanical properties and biocorrosion behaviors of a Mg–Nd–Zn–Zr alloy. J Mech Behav Biomed 2012;7:77–86.

[19] Witte F, Hort N. Degradable biomaterials based on magnesium corrosion. Curr Opin Solid State Mater Sci 2008;12:63–72.

[20] Rosalbino F, Angelini E, De Negri S, Delfino S, Saccone A. Bio-corrosion characterization of Mg–Zn–X (X = Ca, Mn, Si) alloys for biomedical applications. J Mater Sci Mater Med 2010;21:1091–8.

[21] Khan SA, Miyashita Y, Mutoh Y. Influence of Mn content on mechanical properties and fatigue behavior of extruded Mg alloys. Mater Sci Eng A 2006;420:315–21.

[22] Tong LB, Zheng MY, Xu SW, Kamado S, et al. Effect of Mn addition on microstructure, texture and mechanical properties of Mg–Zn–Ca alloy. Mater Sci Eng A 2011;528:3741–7.

[23] Song GL, Song SZ. A possible biodegradable magnesium implant material. Adv Eng Mater 2007;94:298–302.

[24] Zhang E, Yin D, Xu L, et al. Microstructure, mechanical and corrosion properties and biocompatibility of Mg–Zn–Mn alloys for biomedical application. Mater Sci Eng C 2009;29:987–93.

[25] Fu JW, Yang YS. Formation of the solidified microstructure in Mg–Sn binary alloy. J Cryst Growth 2011;322:84–90.

[26] Lu L, Dahle AK, Taylor JA, et al. Theoretical and practical considerations of grain refinement of Mg–Al Alloys. Mater Sci Forum 2005;488–489:299–302.

[27] Du H, Wei Z, Liu X, et al. Effects of Zn on the microstructure, mechanical property and bio-corrosion property of Mg–3Ca alloys for biomedical application. Mater Chem Phys 2011;125:568–75.

[28] Cai S, Lei T, Li N. Effects of Zn on microstructure, mechanical properties and corrosion behavior of Mg–Zn alloys. Mater Sci Eng C 2012;32:2570–7.

[29] Hashemi N, Clark JB. Phase diagrams of binary magnesium alloy. ASM International; 1988.

[30] Lei T, Tang W, Cai SH. On the corrosion behaviour of newly developed biodegradable Mg-based metal matrix composites produced by in situ reaction. Corros Sci 2012;54:270–7.

[31] Choi Y et al. Improvement in corrosion characteristics of AZ31 Mg alloy by square pulse anodizing between transpassive and active regions. Corros Sci 2012. 10.1016/j.corsci.2012.02.010.

[32] Shi Z, Liu M, Atrens A. Measurement of the corrosion rate of magnesium alloys using Tafel extrapolation. Corros Sci 2010;52:579–88.

[33] Argade GR, Kandasamy K, Panigrahi SK, et al. Corrosion behavior of a friction stir processed rare-earth admded magnesium alloy. Corros Sci 2012;58:321–6.

[34] Bakhsheshi-Rad HR, Idris MH, Kadir MRA, Farahany S. Microstructure analysis and corrosion behavior of biodegradable Mg–Ca implant alloys. Mater Des 2012;33:88–97.

[35] Kirkland NT, Birbilis N, Walker J. In vitro dissolution of magnesium–calcium binary alloys: clarifying the unique role of calcium additions in bioresorbable magnesium implant alloys. J Biomed Mater Res 2010;95B:91–100.

[36] Gu XN, Zheng YF. A review on magnesium alloys as biodegradable materials. Front Mater Sci China 2010;4:111–5.

[37] Mao L, Yuan G, Niu J, et al. In vitro degradation behavior and biocompatibility of Mg–Nd–Zn–Zr alloy by hydrofluoric acid treatment. Mater Sci Eng C 2013;33:242–50.

[38] Chun-Yan Z, Rong-Chang Z, Cheng-Long L, et al. Comparison of calcium phosphate coatings on Mg–Al and Mg–Ca alloys and their corrosion behavior in Hank's solution. Surf Coat Technol 2010;204:3636–40.